INTERNATIONAL JOURNAL FOR NUMERICAL METHODS IN ENGINEERING
Int. J. Numer. Meth. Engng 2008; **74**:601–618
Published online 18 September 2007 in Wiley InterScience (www.interscience.wiley.com). DOI: 10.1002/nme.2186

Numerical simulation of smoke clearing with nanoparticle aggregates

N. Zhang[1], Z. C. Zheng[1,*,†] and R. G. Maghirang[2]

[1]*Department of Mechanical and Nuclear Engineering, Kansas State University, Manhattan, KS 66506-5205, U.S.A.*
[2]*Department of Biological and Agricultural Engineering, Kansas State University, Manhattan, KS 66506-5205, U.S.A.*

SUMMARY

Smoke reduction processes in an indoor room-scale chamber are generated by injecting nanoparticle aggregates. A numerical model, with a flow solver implemented with a particle collision model, is used to simulate the smoke-reduction effect. The collision model, developed particularly for simulating collisions among particles with significantly different sizes, enables real-time simulations of three-dimensional, two-phase flow when flow/particle interactions need to be considered. The accuracy of the collision model is estimated by comparing with the exact solution from the Smoluchowski equation. The simulated smoke reduction results are compared with measured data with good agreement. Optimized particle size distributions are studied using the simulation. Copyright © 2007 John Wiley & Sons, Ltd.

Received 30 August 2006; Revised 26 July 2007; Accepted 13 August 2007

KEY WORDS: gas/particle two-phase flow; coagulation; collision model; smoke clearing

1. INTRODUCTION

Aggregates of metal oxide nanoparticles, due to increased surface area, unique morphology, additional functional group on the surface, large porosity, and altered electronic state, have demonstrated effectiveness for inactivation of a wide variety of chemical and biological warfare agents. In addition, they have shown the ability to clear smoke particles in enclosed spaces [1, 2]. Such applications require aerosolization or dispersing of the nanoparticle aggregates (or nano-aggregates) into the affected space. The dispersed nanoparticle aggregates (typically in the size of tens of micrometers) collide with the smoke particles (typically smaller than 3 μm in diameter) and adhere

*Correspondence to: Z. C. Zheng, Department of Mechanical and Nuclear Engineering, Kansas State University, Manhattan, KS 66506-5205, U.S.A.
†E-mail: zzheng@ksu.edu

Contract/grant sponsor: The United States Marine Corps Systems Command to M2 Technologies Inc.

to each other. Because the nanoparticle aggregates have much larger settling velocity than the smoke particles, they will settle to the ground much faster and, therefore, are able to quickly clear the smoke particles in the air.

In order to simulate the smoke reduction effect caused by collisions between smoke particles and nanoparticle aggregates, particle-number density distributions at different particle sizes need to be calculated.

For a homogeneous system, the population balance for the evolution of the particle-number density of Size i particles, n_i, was defined by Smoluchowski [3]:

$$\frac{\mathrm{d}n_i}{\mathrm{d}t} = \frac{1}{2}\sum_{j=1}^{i-1} K_{i-j,j} n_{i-j} n_j - n_i \sum_{j=1}^{\infty} K_{i,j} n_j \tag{1}$$

where $K_{i,j}$ is the collision kernel for collisions between Size i and Size j particles. Note that the volume of a Size i particle is i times the volume of a particle of Size 1. The first term on the right-hand side of Equation (1) accounts for the increase in Size i particles due to collisions of smaller-sized particles, and the second term accounts for losses due to collisions from particles of this size with particles of other sizes.

When using injected nanoparticle aggregates to clear the smoke in an indoor environment, a situation is created of a large number of particles with significantly different sizes. To cover the size range from smallest to largest, millions of different-sized particles are needed, and Equation (1) needs to be solved as many times. For example, if the particle diameter ranges from 1 to 100 μm, then at least 1 million sizes are needed, because the sizes of particles are determined by

$$d_i = i^{1/3} d_1 \tag{2}$$

where d_i is the diameter of a Size i particle. Thus, the computational cost is prohibitively large for a problem in a three-dimensional domain. Although some successful implementations of the above equation have been reported (e.g. [4]), most of them are implemented on a single grid. In unsteady, three-dimensional flow problems such as particle injection into a room-scale chamber, the number of computational grids is at least thousands or even millions. It is thus nearly impossible to solve Equation (1) for particles in all of the sizes on every computational grid at each time step. Therefore, approximating a virtually continuous size spectrum using a set of size classes, or bins, is very much needed in reality. The idea was first put forth by Gelbard and Seinfeld [5]. In the simulation by Lawler *et al.* [6], a weighting function is introduced to distribute coagulated particles whose sizes are between two consecutive bins into each of these two bins. Later, the idea of bin structures was implemented by several other researchers, including Jacobson *et al.* [7], Fernandez-Diaz *et al.* [8], and Sandu [9]. In these three implementations, it is assumed that the particle-number density inside one volume bin is uniform and the volume ratio of two adjacent bins has to be small enough (e.g. <1.5, as shown in Figure 2 in [7]) to provide accurate results.

The collision model used in this study is designed for simulating practical gas/particle multiphase flow problems. For the problem in this study which requires a large number of three-dimensional computational grids with turbulence, the simulation of flow phase is already expensive. For the particulate phase, the number of equations is determined by the number of bins. It is therefore necessary to reduce the bin number to the minimum, i.e. to increase the volume ratio of two adjacent bins to the maximum. For this purpose, several modifications and approximations have been made to Equation (1). In the current method, larger sizes of bins can be used without losing desired accuracy due to the fact that the collision simulation is for particles with significantly different

DOI: 10.1002/nme

sizes. In using nanoparticle aggregates to reduce smoke in a chamber, relatively large particles are injected into a chamber to 'capture' very small smoke particles. Since the size difference is large between the nano-aggregates and smoke particles, the effect of collision between same-sized particles is negligible compared with the collisions between different-sized particles. The continuous bin structures between the small and large particles are very wasteful in this problem. The current method uses the discontinuous bin structures, thereby reducing the computational cost significantly. Simulation results using this model are compared with the exact solutions from the Smoluchowski [3] equation, Equation (1), to validate the model.

Because the computational overhead of the simulation is reduced significantly by using this modified collision model, the collision simulation can be integrated in a three-dimensional unsteady turbulent flow solver to simulate the smoke-reduction effect. The smoke-reduction simulation results are compared with the experimental measurement data. The simulation model is further applied for the purpose of determining the optimal injection particle sizes for smoke reduction.

2. DESCRIPTION OF THE COLLISION MODEL

While Equation (1) represents a population balance in terms of particle numbers, the basic assumption adopted in the present coagulation method is that the total mass of all of the bins is conserved. All the particles considered are assumed spherical. When the collisions occur, the mass lost in certain bins of particles is equal to the mass increase in the other bins of particles. This mass balance can be written as

$$\frac{\mathrm{d}\rho_i}{\mathrm{d}t} = \sum_{j=1}^{i-1} \Delta\rho_{j \text{ loss to } i} - \sum_{j=1}^{\infty} \Delta\rho_{i \text{ loss to } j} \tag{3}$$

where ρ_i is the mass of the Size i particles, and is defined as

$$\rho_i = w_i n_i = \tfrac{1}{6}\pi d_i^3 \gamma_i n_i \tag{4}$$

where w_i (kg/count) and γ_i are the weight of an individual particle and material density of Size i particles, respectively. Equation (3) represents the change of mass per time for Size i particles. The first term on the right-hand side of Equation (3) is the mass gain due to collisions of smaller-sized particles, while the second term accounts for the mass loss of current-size particles due to collisions between current size and other sizes. The mass loss in one size is accounted for by the mass increase in the other sizes. The expression for $\Delta\rho_{j \text{ loss to } i}$ will be determined later.

If we consider mass balance among volume bins instead of among particle sizes, Equation (3) still stands, with the index i now denoting Bin i instead of Size i, and ρ_i represents the mass of Bin i. At this point, an additional variable needs to be introduced, the volume ratio between two bins,

$$V_{i,j} = \frac{v_i}{v_j} = \frac{d_i^3}{d_j^3} \tag{5}$$

where v_i is the volume of particles in Bin i. If $V_{i,j}$ is constant between two consecutive bins, by denoting this ratio as V_{ratio}, we have

$$V_{\text{ratio}} = \frac{v_{i+1}}{v_i} \tag{6}$$

DOI: 10.1002/nme

For any values of V_{ratio} greater than one, the volume of a Bin i particle is

$$v_i = v_1 V_{\text{ratio}}^{i-1} \tag{7}$$

and its radius is

$$r_i = r_1 V_{\text{ratio}}^{(i-1)/3} \tag{8}$$

Consequently, from Equation (8), it can be deduced that the number of bins that covers the particle-size range from radius r_1 to r_i is

$$i = 1 + \ln[(r_i/r_1)^3]/\ln[V_{\text{ratio}}] \tag{9}$$

In realistic applications, the ratios between two consecutive bins may not always be constant.

If V_{ratio} is large, the two adjacent bins have a wide size difference. Therefore, when collisions occur between a bin of small particles (small bin) and a bin of large particles (large bin), we assume that the resulting particles will fall into the large bin instead of falling into the next larger bin. That is, the mass loss from the small bin equals the mass increase in the large bin. When these types of collisions occur, the mass loss in a bin is incurred only when the particles in this bin collide with particles in larger bins. The mass loss in Bin j is, based on Equation (1),

$$\Delta\rho_{j \text{ loss to } i} = w_j \Delta n_{j \text{ loss to } i} = w_j K_{i,j} n_i n_j \tag{10}$$

Hence, the addition in Bin i is

$$\sum_{j=1}^{i-1} \Delta\rho_{j \text{ loss to } i} = \sum_{j=1}^{i-1} w_j K_{i,j} n_i n_j \tag{11}$$

The summation in Equation (11) corresponds to the overall gain in Bin i due to collisions with all of the smaller bins. Based on the definition of w_i in Equation (4) and on Equation (5), we can obtain

$$w_j = V_{j,i} w_i \frac{\gamma_j}{\gamma_i} = \frac{w_i}{V_{i,j}} \frac{\gamma_j}{\gamma_i} \tag{12}$$

Hence, Equation (11) becomes

$$\sum_{j=1}^{i-1} \Delta\rho_{j \text{ loss to } i} = \sum_{j=1}^{i-1} \frac{\gamma_j}{\gamma_i V_{i,j}} w_i K_{i,j} n_i n_j \tag{13}$$

On the other hand, the mass loss in Bin i, which is due to collisions only between Bin i particles and particles in the bins larger than Bin i, can be expressed by using Equation (10) as

$$\sum_{j=i+1}^{\infty} \Delta\rho_{i \text{ loss to } j} = \sum_{j=i+1}^{\infty} w_i \Delta n_{i \text{ loss to } j} = \sum_{j=i+1}^{\infty} w_i K_{j,i} n_j n_i \tag{14}$$

Note that the summation in the above equation starts at $i+1$, indicating that the mass loss is only caused by collisions that occurred between the current bin and the larger bins. Substituting Equations (11) and (14) into Equation (3), we have

$$\frac{\mathrm{d}\rho_i}{\mathrm{d}t} = \frac{\mathrm{d}(w_i n_i)}{\mathrm{d}t} = \sum_{j=1}^{i-1} \frac{\gamma_j}{\gamma_i V_{i,j}} w_i K_{i,j} n_i n_j - \sum_{j=i+1}^{\infty} w_i K_{j,i} n_j n_i \tag{15}$$

DOI: 10.1002/nme

Since w_i does not change with time, Equation (15) can be simplified to yield, in terms of particle-number density,

$$\frac{\mathrm{d}n_i}{\mathrm{d}t} = n_i \sum_{j=1}^{i-1} \frac{\gamma_j}{\gamma_i V_{i,j}} K_{i,j} n_j - n_i \sum_{j=i+1}^{\infty} K_{i,j} n_j \tag{16}$$

The first term on the right-hand side of Equation (16) accounts for addition from smaller bin particles colliding with current bin particles, while the second term accounts for the loss of current bin particles colliding with particles in larger bins. This equation is based on the assumption that all collisions within one bin can be neglected. In other words, collisions among particles within the same bin would not generate particles large enough to jump into the next larger bin. Under this assumption, although the number or the average size of particles in this bin may change due to the inner-bin collision, the total mass of this bin still remains the same.

It should be noted that since Equation (16) can be re-written as

$$n_i(t) = n_i(0) * \exp\left[\int_0^t \left(\sum_{j=1}^{i-1} \frac{\gamma_j}{\gamma_i V_{i,j}} K_{i,j} n_j - \sum_{j=i+1}^{\infty} K_{i,j} n_j\right) dt\right] \tag{17}$$

the value of n_i remains zero if initially n_i at $t=0$ is zero. Therefore, Equation (16) works well only in those applications where the differences in particle sizes are very large and the bins are discontinuous, such as in the smoke-reduction application, when very large particles are injected to capture very small smoke particles. The results of the smoke-reduction application will be presented in the next section.

A validation case has been facilitated to compare the results from Equations (16) and (1). The result using Equation (1) is considered the 'exact' solution. The case is for two groups of significantly different sizes of particles, with initially mono-sized particles in each group. The particles are confined in a cube of $1\,\mathrm{m}^3$ that has no mass in and no mass out; hence, the total mass is conserved. There are a total of 550 consecutive sizes to be included in the exact simulation, from Size 1 to size 550. At the beginning of the simulation, the nonzero-number particles, with substantially different sizes as the intended model case, are selected Size 1 and size 64. All the other sizes are initially with zero particle number. The particles are of the same material so that the material density is the same for different-sized particles. The initial particle-number densities are specified as $n_{\mathrm{size1}} = 1 \times 10^{12}\,\mathrm{count/m}^3$ and $n_{\mathrm{size64}} = 1.5625 \times 10^{10}\,\mathrm{count/m}^3$, and zero for the other sizes. The reason for selecting the value of n_{size64} is to match the same mass as Size 1. The physical diameter of Size 1 particles is specified as $1\,\mu\mathrm{m}$ so that the physical diameter of Size 64 particles is $4\,\mu\mathrm{m}$, according to Equation (2).

When applying the present model for simulation to compare with the above-described exact simulation, three bins are used: Bin 1 to include Sizes 1–7 particles; Bin 2 to include Sizes 8–63; and Bin 3 to include Sizes 64–511. Although the largest particle size is 511 following the bin-volume ratio of 8 with the three bins, the upper limit size of the exact simulation is selected to be 550 to ensure sufficient numerical buffer sizes between 511 and 550 in using Equation (1).

The initial particle-number density in each of the bins becomes

$$n_{\mathrm{bin1}} = \sum_{i=1}^{7} n_{\mathrm{size}_i} \tag{18}$$

DOI: 10.1002/nme

$$n_{\text{bin2}} = \sum_{i=8}^{63} n_{\text{size}_i} \tag{19}$$

and

$$n_{\text{bin3}} = \sum_{i=64}^{511} n_{\text{size}_i} \tag{20}$$

Therefore, from the initial condition for the exact simulation, the corresponding initial condition for the bin model becomes $n_{\text{bin1}} = n_{\text{size1}}$, $n_{\text{bin2}} = 0$, and $n_{\text{bin3}} = n_{\text{size64}}$. Note that in the exact equation, Equation (1), the particle-number density is for each size, while in the bin model, Equation (16), the particle-number density is for each bin. A constant volume ratio between the two consecutive bins, $V_{\text{ratio}} = 8$, is used. The representative diameters of the particles in each of the bins are 1, 2, and 4 μm, respectively.

A homogeneous, isotropic, constant-intensity turbulence is specified as the background turbulence for the collision mechanism. The Saffman–Turner collision kernel [10] is used in the simulation as

$$K_{(\text{turb})i,j} = \left(\frac{8\pi}{15}\right)^{1/2} \frac{a_{i,j}^3}{t_k} \tag{21}$$

where $a_{i,j}$ is the collision diameter defined as $r_i + r_j$, and t_k is the Kolmogorov time scale defined as $(\nu/\varepsilon)^{1/2}$ with ν and ε to be, respectively, the kinematic viscosity and the turbulence dissipation rate. In this test case, a relatively strong turbulence level is specified, resulting in the constant part in Equation (21) to be

$$\left(\frac{8\pi}{15}\right)^{1/2} \frac{1}{t_k} = 1000(1/\text{s}) \tag{22}$$

The total simulated time is 1 min and the time step is 0.05 s. A first-order Euler scheme is used for time marching. This scheme is selected for its simplicity of coding and easy implementation later with the fluid flow solver. The accuracy of the selected time step has been tested by comparing the results using a time step of 0.1 s and showing negligible differences. Figure 1 shows the evolution histories of the mass of each bin. The ordinate in Figure 1 is the volume fraction of each bin particle in the cube. Because all the particles are of the same material, the volume fraction can be used as indicative of mass balance among the bins. Since the results of the exact solution are for each size, for the purpose of comparison, we combine the total mass in Sizes 1–7 to represent the mass of Bin 1, Sizes 8–63 for Bin 2, and Sizes 64–511 for Bin 3. It is clear that the present model matches the exact solution perfectly, because the two Bin 3 lines match perfectly and overlap each other, as do the two Bin 1 lines (and that is why there are only four distinguishable curves with six legends in Figure 1). The mass of Bin 1 decreases while the mass of Bin 3 increases, justifying the assumption that the collisions between the small-bin particles and the large-bin particles lead to the resulting particles falling into the large bin. According to the wide-bin-width assumption in the present model, since the particle-number density of Bin 2 is originally zero, it would remain zero in this bin all the time in the results of this model, as expressed in Equation (17). It is also evident from the results of the exact simulation that the value of particle-number density in Bin 2 is very small (close to zero), with a value of particle-number density approximately 8 orders of

DOI: 10.1002/nme

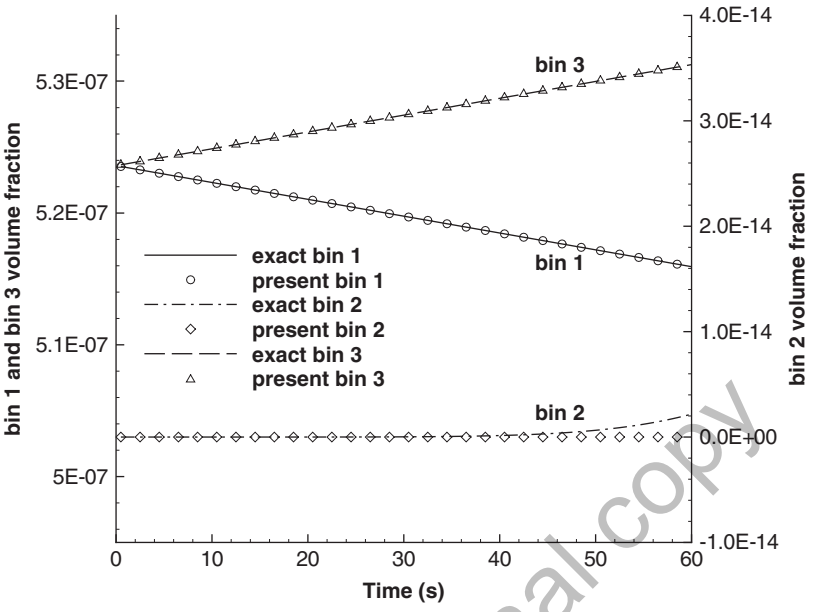

Figure 1. Time history comparison of total mass in each bin between the present model and the exact solution.

magnitude smaller than those in the other bins even after a minute of simulation time. That means that the inner-bin collisions in Bin 1 are unlikely to generate particles large enough to jump to the next bin if the bin width is wide.

3. PREDICTIONS OF SMOKE-REDUCTION EFFECT

Before the discussion of the flow and particulate phase equations used in this application, the collision kernel, $K_{i,j}$, used in the simulation needs to be defined. In the smoke-reduction application, the collision is induced by two effects: one is turbulence and the other is differential sedimentation. The turbulence collision kernel used here is from [10], as expressed in Equation (21). The differential-sedimentation–collision kernel is from [11]

$$K_{(\text{sed})i,j} = \pi a_{i,j}^2 (U_{\text{sett},i} - U_{\text{sett},j}) \quad \text{if } i > j \tag{23}$$

where $U_{\text{sett},i}$ is the settling speed for particles of Size i. The differential sedimentation collision is induced by the difference in settling speeds when larger particles with a faster settling speed catch smaller particles with a slower settling speed in the path of the settling. Note that the differential-sedimentation–collision effect is not significant when particle sizes are similar. Combining Equations (21) and (23), the total collision kernel becomes

$$K_{i,j} = K_{(\text{turb})i,j} + K_{(\text{sed})i,j} \tag{24}$$

DOI: 10.1002/nme

The air/solid-particle flow problem is simulated using an Euler-type formulation for both the air flow and the particulate phase. The continuous air-flow phase is governed by the unsteady compressible flow equations

$$\frac{\partial \rho}{\partial t} + \nabla \cdot (\rho \mathbf{u}) = 0 \tag{25}$$

and

$$\rho \frac{\mathrm{D}\mathbf{u}}{\mathrm{D}t} = -\nabla p + \nabla \cdot \bar{\bar{\tau}} \tag{26}$$

where the body force, either due to the gravitational acceleration or arising from interactions with the solid particles, is neglected because of the small particle sizes considered. The Kolmogorov length scales in this problem for turbulent flow are also relatively large in comparison with all the particle sizes. It is therefore assumed that the air flow affects the particulate phase significantly, while the behavior of the particulate phase does not impose any effect on the air flow. The one-way interaction assumption is also justified by the light-loading particulate phase considered here [12].

The collision model discussed in the previous section is used to include the collision effect. There are two reasons to justify the use of this collision model. First, the difference in size between the injecting particles and smoke particles in this study is large. Second, the collision kernel used allows for neglecting the inner-bin collision. During much of the smoke-reduction process, the differential-sedimentation–collision effect is dominant in the collision kernel. The particles within the same bin are similar in size and thus have similar settling speeds. As a result, the collision kernel, $K_{i,i}$, calculated from Equation (23) between two similar-sized particles is close to zero, and therefore the inner-bin collision effect is minimal. The particulate phase transport equation can be written as

$$\frac{\partial n_i}{\partial t} + \nabla \cdot (\mathbf{u} n_i) = -\mathbf{U}_{\mathrm{sett}} \cdot \nabla n_i + \nabla \cdot (D_{\mathrm{d}} \nabla n_i) + \sum_{j=1}^{i-1} \frac{\gamma_i}{\gamma_j V_{i,j}} K_{i,j} n_i n_j - n_i \sum_{j=i+1}^{\infty} K_{i,j} n_j \tag{27}$$

where D_{d} is the diffusivity (both laminar and turbulent) of the particles in air and $\mathbf{U}_{\mathrm{sett}}$ is the particle settling speed, defined as

$$\mathbf{U}_{\mathrm{sett}} = C_{\mathrm{c}} \tau_{\mathrm{p}} \mathbf{g} \tag{28}$$

In Equation (28), C_{c} is the slip correction factor [13], $\mathbf{g}$ is the gravitational acceleration, and τ_{p} is the particle relaxation time defined as

$$\tau_{\mathrm{p}} = \frac{\rho_{\mathrm{p}} d_{\mathrm{p}}^2}{18\mu}$$

The diffusion coefficient in Equation (27), D_{d}, combines the laminar and turbulent diffusion parts, D_{l} and D_{t}. The laminar diffusion coefficient is calculated using the Stoke–Einstein equation [13]

$$D_{\mathrm{l}} = \frac{kTC_{\mathrm{c}}}{3\pi\mu d_{\mathrm{p}}} \tag{29}$$

DOI: 10.1002/nme

where k is the Boltzmann constant, 1.38×10^{-23} (N m/K), T is the absolute temperature, C_c is the slip correction factor, and μ is the dynamic viscosity of the air. The turbulent diffusion coefficient is defined by

$$D_t = \frac{v_t}{Sc_t} \tag{30}$$

where v_t is the turbulent viscosity and Sc_t is the turbulent Schmidt number. The turbulent Schmidt number measures the relative diffusion of momentum and mass due to turbulence and is on the order of unity in all turbulent flows. Because it is an empirical constant that is relatively insensitive to the molecular fluid properties, Sc_t is set to be 0.7 [14] for all the cases.

Note that in obtaining Equation (27), the small-slip continuum model [15] is applied, which is compatible with the one-way flow–particle interaction assumption. The boundary condition requirements in the particulate phase, for each of the convection, diffusion, and settling effects, were studied previously [16]. The values of the volume ratio, $V_{i,j}$, will be determined based on each case discussed in the following subsections.

In the solution procedure, the FLUENT flow solver with the realizable k–ε turbulence model [17] is used to solve Equations (25) and (26), because of the better behavior of this model than a standard k–ε model for low Reynolds number flow. The primary reasons for using a realizable k–ε model are (1) to introduce a variable model coefficient, C_μ, to avoid the negative normal Reynolds stress and (2) to completely remove the well-known spreading rate anomaly of planar and round jets [17]. For the problem studied here, these are the two possible sources of errors from the standard k–ε model. Nevertheless, we also performed tests comparing these two turbulence models, and there were no noticeable differences found in the particle-number density distribution. Moreover, since the jet lasts only 2 s in the studied problem, turbulence decreases quickly after the jet stops. Therefore during most of the simulation time, turbulence has little influence on the particulate phase.

The computational scheme is second order in time and space. The second-order upwind scheme is used for the convection terms, and the second-order central differencing method is used for the diffusion terms. Once the flow-field solutions are obtained, the velocity field is input to the particulate phase computing subroutines to solve Equation (27). In solving the particulate phase transport equation, Equation (27), a passive scalar transport equation solver in FLUENT is used with some modifications. For a passive scalar ϕ_i, a general convection–diffusion equation

$$\frac{\partial \rho\phi_i}{\partial t} + \nabla\cdot(\rho\mathbf{u}\phi_i) - \nabla\cdot(\Gamma_i\nabla\phi_i) = S_i \quad (i=1,\ldots,N) \tag{31}$$

can be solved in FLUENT using similar schemes in the flow solver, where Γ_i and S_i are the diffusion coefficient and the source term that can be supplied by the user for each of the N scalar equations.

In order to make use of the solver for Equation (31), Equation (27) can be re-written as

$$\frac{\partial n_i}{\partial t} + \nabla\cdot[(\mathbf{u}+\mathbf{U}_{sett})n_i] - \nabla\cdot(D_d\nabla n_i) = \sum_{j=1}^{i-1}\frac{\gamma_i}{\gamma_j V_{i,j}}K_{i,j}n_i n_j - n_i\sum_{j=i+1}^{\infty}K_{i,j}n_j \tag{32}$$

In this format, D_d is calculated as Γ_i in Equation (31) with a user-defined function (UDF) called 'DEFINE_DIFFUSIVITY' to calculate the diffusion coefficient on every grid point of the computational domain. The diffusion terms are then discretized using the second-order central differencing.

DOI: 10.1002/nme

The collision terms, which are the right-hand-side terms in Equation (32), are implemented as the source term S_i using the UDF 'DEFINE_SOURCE.' The source term is handled explicitly.

Further, comparing the format of Equation (32) with that of Equation (31), it can be seen that modifications are needed for the convection and unsteady terms. The convection and settling terms of Equation (32) are combined as the convection term and is solved implicitly. The convection term in its original scalar transport equation, Equation (31), has the following general form:

$$\nabla \cdot \boldsymbol{\psi} \phi_i$$

where $\boldsymbol{\psi}$ is a vector field. In the default convection term in Equation (31), $\boldsymbol{\psi}$ is the product of the density and the velocity vector:

$$\boldsymbol{\psi}_{\text{default}} = \rho_{\text{f}} \mathbf{u} \tag{33}$$

where ρ_{f} is the density on the cell face. Note that $\boldsymbol{\psi}_{\text{default}}$ values on all cell faces are automatically computed during the procedure in solving the flow in FLUENT and can be directly accessed by the user. To define the convection term using the UDF 'DEFINE_UDS_FLUX', the user needs to return the scalar value $\boldsymbol{\psi} \cdot \mathbf{A}$ to FLUENT, where $\mathbf{A}$ is the face normal vector of the cell face. $\mathbf{A}$ vales of all cell faces are calculated by FLUENT and can be accessed. Since there is no ρ in Equation (32) and the settling term is added, the returned $\boldsymbol{\psi} \cdot \mathbf{A}$ becomes

$$\boldsymbol{\psi} \cdot \mathbf{A} = \boldsymbol{\psi}_{\text{default}} \cdot \mathbf{A} / \rho_{\text{f}} + \mathbf{U}_{\text{sett}} \cdot \mathbf{A} \tag{34}$$

Because only the ρ value of the cell is recorded in the flow solver, the face value ρ_{f} is calculated as the average of two neighboring cell values. The convection terms are discretized using the second-order upwind scheme.

Finally, for the unsteady term in the scalar transport equation, the only modification required is to re-define the coefficients of the unsteady term to remove the density in the default format. The solver expects that the unsteady term is decomposed into an implicit and an explicit component. For the finite-volume scheme with a first-order march in time, we have

$$\int \frac{\partial n_i}{\partial t} \, \mathrm{d}V = \frac{\Delta V}{\Delta t} n_i^m - \frac{\Delta V}{\Delta t} n_i^{m-1} \tag{35}$$

where ΔV represents the volume of the cell and m represents the current time step. In the UDF 'DEFINE_UDS_UNSTEADY,' the coefficient of the implicit term (the n_i^m term) and the whole explicit term are the two variables to be input to the solver. Therefore, the above computational scheme of the particulate phase using Equation (27) or (32) is first-order accurate in time and second-order accurate in space.

Figure 2 illustrates the chamber geometry in the simulation whose spatial dimension is $3.7\,\text{m} \times 2.4\,\text{m} \times 2.4\,\text{m}$ in the x, y, and z directions, respectively. A $96 \times 64 \times 64$ grid mesh is placed in the three-dimensional computational domain. Higher and lower resolution grids were also tested to determine the necessary resolution for grid-independent simulations. The particles are deployed through one of the inlet ports with a velocity of 40 m/s. The injection lasts 2 s. The location of the inlet port A is at the upper left quadrant 0.6 m from the left-end wall ($x = 0.6$) and 0.4 m from the ceiling ($z = 2.0$); the inlet port B is located in the right-end wall ($x = 3.7$) and at the center of the wall ($y = 1.2$) and 0.57 m from the ceiling ($z = 1.83$). Detailed descriptions of the injection and measurement setup are presented in [12]. Validations of particle deposition and spatial distribution showed good agreement with the measured data [12].

DOI: 10.1002/nme

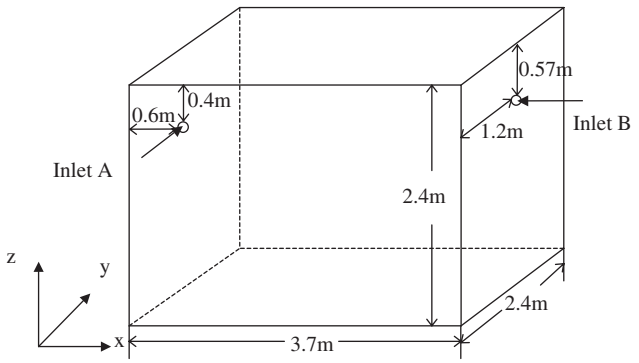

Figure 2. Illustration of the chamber and the particle injection ports, and the coordinate system used in the simulation.

3.1. Comparison with measured data in a smoke-reduction experiment: injection with wide-range-sized particles

In this section, a validation of the smoke-reduction simulation results using experimental data is carried out. The smoke-reduction measurement was performed in the same chamber as illustrated in Figure 2. Initially, the chamber was filled with glycol smoke uniformly. The glycol smoke served as a simulant of smoke. It is used in theatrical productions to simulate battle smoke and fires. The glycol aerosol was generated with a commercially available smoke generator. The generator had a heating element through which the glycol/water solution was pumped and vaporized. Upon exiting the generator nozzle, the vapor condensed rapidly to form a dense visible aerosol. The mass concentration of the smoke, when the light transmission through the chamber was zero, was approximately $150\,\mathrm{mg/m^3}$. The aerodynamic geometric mean diameter of the smoke, as measured with an 8-stage cascade impactor, was approximately $2.5\,\mu\mathrm{m}$. The material density of smoke particle was $1\,\mathrm{g/cc}$.

Nanoparticle powders in this research are the large nanoparticle aggregates of the size of tens of micrometers. The metal oxide nanoparticle aggregates used in the experiment were MgO+, produced by NanoScale Material, Inc. The nanoparticle aggregates were dispersed into the chamber using a pressurized canister and lasted approximately 2 s through either port A or port B shown in Figure 2. The total mass injected into the chamber was approximately 52.3 g. The size of the nanoparticle aggregates ranged from 5 to $140\,\mu\mathrm{m}$. The total mass concentration of the smoke and dispersed nano-aggregates near the center of the chamber was recorded using a tapered element oscillating microbalance (TEOM), a device for continuously monitoring the mass concentration of airborne particulate matter.

In the simulation, five bins of particles are allocated to represent the smoke and injected particles, and they are 2.5 (smoke), 10, 20, 40, and $90\,\mu\mathrm{m}$. The volume ratios between the five bins, calculated using Equation (5), are listed in Table I, where the first row lists the diameter of Bin i particles, and the first column lists the diameter of Bin j particles. Each value of ratio in the table is v_i/v_j in Equation (5) calculated according to the diameters.

Since there is no particle-size-distribution measurement at the inlet, there is no measured inlet particle-number density to be used for the inlet boundary condition for simulation. One way to find the approximate mass percentage of particles in each bin in the total 52.3 g injected mass is

DOI: 10.1002/nme

Table I. Volume ratios between particles of two bins (v_i/v_j).

$j\backslash i$	2.5 μm	10 μm	20 μm	40 μm	90 μm
2.5 μm	1	64	512	4096	46 656
10 μm	1/64	1	8	64	729
20 μm	1/512	1/8	1	8	91.13
40 μm	1/4096	1/64	1/8	1	11.39
90 μm	1/46 656	1/729	1/91.13	1/11.39	1

Table II. Injected particle properties and inlet boundary conditions.

Bin size (μm)	Mass (g)	Inlet n (count/m^3)	Settling velocity (m/s)
10 (<15)	5	2.0E+11	0.001214
20 (15–30)	12	6.0E+10	0.004856
40 (30–60)	15	9.4E+09	0.019424
90 (>60)	20	1.1E+09	0.098334

to compare with the deposition measurement data [12]. We counted the total number of particles of each size range in the whole experimental period, and then calculated the mass ratios among different size ranges. Table II shows the mass for each bin particle and the corresponding inlet particle-number density. Moreover, it was difficult to conduct measurement on the small area of the injection port where the flow speed was high.

Figure 3 shows the comparison of the time history of the total mass concentration of all sizes of particles at the center of the chamber. Because of the uncertainty with the inlet boundary condition, an exact match between the simulation result and experimental measurement is not expected. Because of differences between the injection particle distribution and the distribution on the floor, which can cause errors in the simulation, the mismatch between experiment and simulation shown in Figure 3 is particularly significant in the initial period, where the simulation result over-predicts the mass concentration at the first point (1 min). After that, the agreement with the experimental data is relatively good. In both simulation result and experimental data, the decaying trend of the total mass concentration can be clearly identified. Both curves become flat after about 10 min. This is because after 10 min only a small number of injected particles are left in the chamber. At the end of 20 min, the simulation result tends to over-predict the mass concentration a little compared with the experimental data. Finally, Figure 3 also shows that the mass concentrations from both results are not less than the initial mass concentration even after 20 min, which indicates that under this injection configuration, the smoke reduction is not very effective. In addition to the particle properties, the ineffectiveness could also be attributed to the injection method used in the case [12], a factor that requires further investigations.

3.2. Optimized particle sizes for smoke reduction: simulation for mono-sized particle injection

From the results of the smoke-reduction experiment described in Section 3.1, the smoke-reduction effectiveness is not significant. This effectiveness depends on many factors, such as particle sizes, injection mass, processing time, and injection methods. These factors are in many cases inter-related. In addition, there are a variety of ways to achieve smoke reduction. In this paper, the focus

DOI: 10.1002/nme

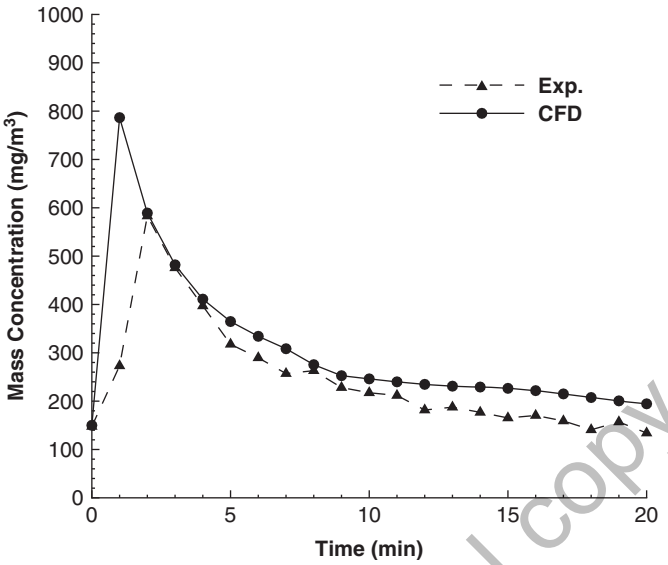

Figure 3. Time history comparison of total mass concentration at the center of the chamber with the experimental measurement.

is on particle size. The purpose is to find optimal injecting particle sizes that can be incorporated with other methods to achieve the desired effectiveness.

When a fixed amount of mass of nano-powder is injected, the settling velocity and the number of particle powders are determined by the size of powders. The settling velocity determines the settling time, while the number of particles determines the number of smoke particles captured. If the powder particle size is large, the settling velocity is large; however, on the other hand, the number is small so that only a small portion of smoke can be captured. On the contrary, if the particle size is small, more numbers of particles are in the fixed amount of powder mass, and thus more smoke particles can be captured. But these particles have smaller settling velocity, which means longer time for them to drop to the ground. Therefore, one of the purposes of this research is to find the optimal injecting powder sizes based on different smoke-reduction requirements.

While it is obvious that only a limited amount of mass of nano-powder can be injected under a specific powder–smoke mass ratio, the optimal size also varies. Hence, the other purpose of this research is to find the relationship between optimal powder size and injection mass.

To determine the optimal injecting particle size, several test cases have been simulated. The same room-scale chamber as shown in Figure 2 is specified in the simulation. The injection location of all the test cases is through inlet port B. The size of the smoke particle selected is 2.5 μm, while three injected particle sizes in three test cases are 10, 30, and 90 μm. In these three mono-sized injection cases, two volume bins are used, and the volume ratio in each case is determined by the size of injected nanoparticles and the size of smoke particles, following Equation (5). The volume ratios between injected particles and smoke particles are thus 64, 1728, and 46 656 for the 10, 30, and 90 μm injection cases, respectively.

The total mass of smoke particles in the chamber is 10 g, resulting in an initial smoke particle-number density inside the chamber of $n_{\text{smoke}} = 5.62 \times 10^{10}$ (counts/m^3). The total mass of particles

DOI: 10.1002/nme

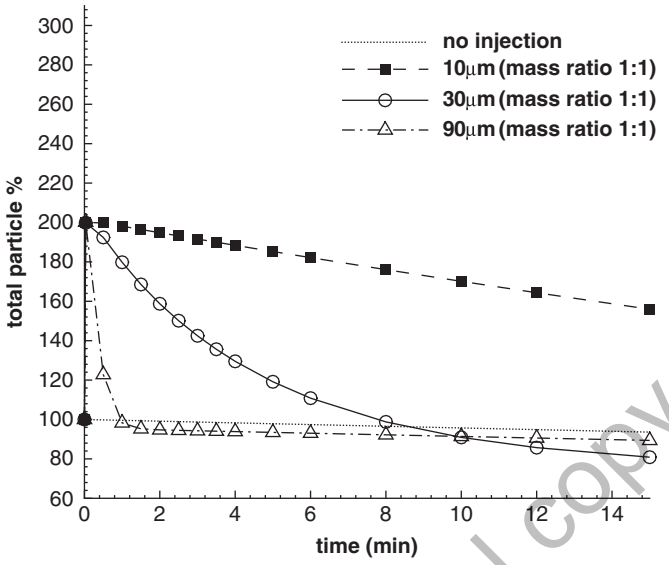

Figure 4. Time history comparison of total mass concentration for the case with the injection–smoke mass ratio of 1.

injected into the test chamber for each test case is also 10 g. Thus the inlet boundary conditions of n for three injection cases are $n_{10\,\mu m} = 4.01 \times 10^{11}$ (counts/m^3), $n_{30\,\mu m} = 1.49 \times 10^{10}$ (counts/m^3), and $n_{90\,\mu m} = 5.50 \times 10^{8}$ (counts/m^3). The total test time is 15 min.

Figure 4 is the time history comparison of total mass in the chamber among test cases of 10, 30, 90 μm, injection, and no injection. The percentage value in the plot is the ratio of current mass to the initial smoke mass. The plot shows that two of the three injection cases (30 and 90 μm) have better smoke-reduction effects than the no-injection case. Without injecting particles, the settling velocity of the smoke particle is very small. After 15 min, there is still 94% of smoke left in the chamber; hence, the total smoke-reduction capability in 15 min is 6%. The 10 μm injection case is worse than the no-injection case in smoke reduction, because the total particle mass, after 15 min, is even more than the initial smoke mass. This is because when the size of injected particles is close to that of smoke particles, the injected particles themselves need a very long settling time. Therefore, this size is not very meaningful in the smoke-reduction applications. Between the 30 and 90 μm cases, after 15 min, the 30 μm case shows the best result in the smoke-reduction capability, about 19% reduction. The 90 μm case is the second best with about 11% reduction. From the point of view of total smoke-reduction capability in 15 min, the 30 μm size is the optimal size. However, also shown in Figure 4 is that from 1 min to about 10 min, the 90 μm particles perform better than the 30 μm particles, while the performance of the 30 μm particles exceeds that of the 90 μm particles after 10 min. For the 90 μm case, since the settling speed of 90 μm particles is the fastest, during the first few minutes, the smoke-reduction effect is the best. However, because the number of 90 μm particles in 10 g of mass is the smallest in the three cases, they can only capture the least number of smoke particles so that the total smoke-reduction effect in 15 min is not the best. It can thus be concluded that if time is a concern, the 90 μm size is probably the optimal size. Otherwise, the 30 μm size is optimal. The 30 μm size particles have a relatively fast settling speed

DOI: 10.1002/nme

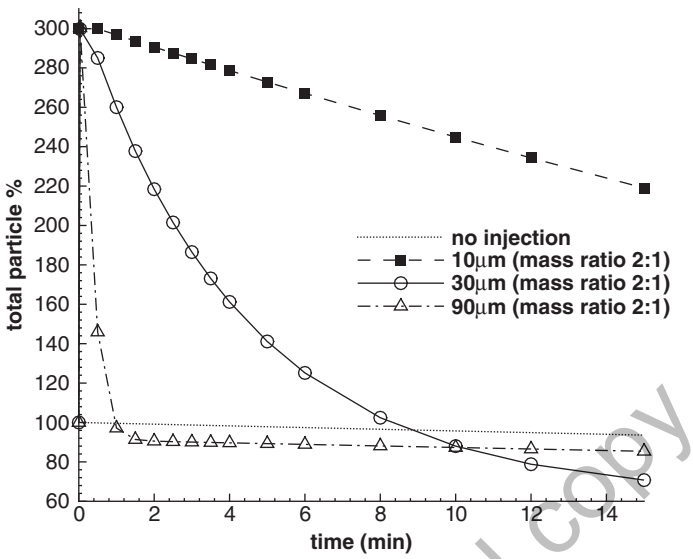

Figure 5. Time history comparison of total mass concentration for the case with the injection–smoke mass ratio of 2.

and a modest particle number; hence, they are able to capture the most number of smoke particles in a certain amount of time.

There is one more criterion that is used to determine the performance of smoke reduction, the deterioration time during which the total mass of the airborne particles in the chamber is more than that with no injection. The deterioration time of the 90 μm injection (1 min) is much shorter than the 30 μm case (8.5 min). From the aspect of the deterioration time, the 90 μm case is better.

It should be noted that the comparison shown in Figure 4 is under an important condition, i.e. the injected mass equal to the smoke mass in the chamber. If more mass can be injected into the chamber, will all the sizes perform differently from the previous tests? To answer this question, comparisons among the 10, 30, and 90 μm particles are conducted when 20 g of mass is injected. Figure 5 shows the smoke-reduction effects of these three sizes in the period of 15 min under the 2:1 injection mass–smoke mass ratio (20 g:10 g). The total smoke-reduction capabilities increase in the 30 μm and 90 μm cases and decrease in the 10 μm case. However, the time period when the 90 μm case is better than the 30 μm case has been slightly prolonged compared with the 1:1 mass ratio case. The 90 μm is better than the 30 μm until a little after 10 min. Then the 30 μm takes over to show better performance. As for the deterioration time, it is also increased by 0.5 min for the 30 μm case but almost unchanged for the 90 μm case.

It can be concluded that the optimal particle size of the injection is determined by many factors, including mass, reduction capability, and time. For a certain amount of mass of injected particles, the smoke-reduction capability is better when small particles are used than larger particles because of more particle numbers in the same mass of small particles. However, the time needed to reach that capability is longer for small particles due to the low settling speed. So the trade-off between capability and time determines the optimal size. If the injected mass is increased, the total capability will increase due to the increased number of injected particles. One can inject more mass of larger

DOI: 10.1002/nme

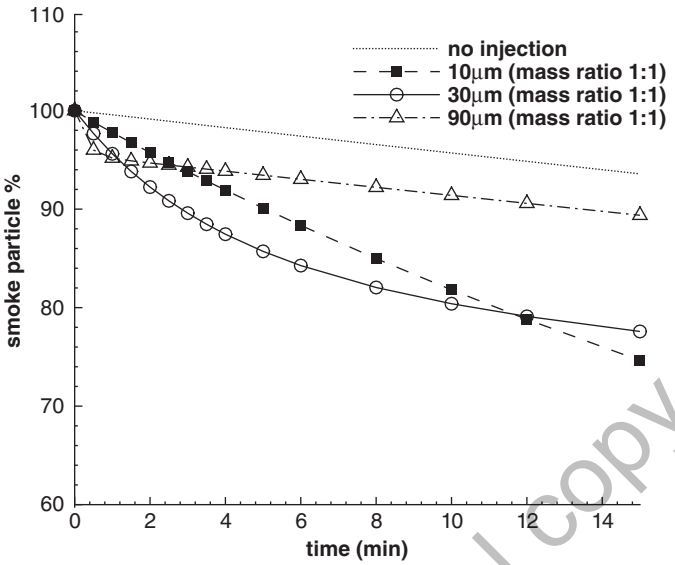

Figure 6. Time history comparison of smoke mass concentration for the case with the injection–smoke mass ratio of 1.

particles to achieve the same smoke-reduction result by using less mass of smaller particles, but with much shorter time. When injecting more mass, the time during which large particles perform better than small particles in smoke reduction is prolonged. By combining the factors discussed above, it can be claimed that the size of the optimal particles increases with the increase in injected mass.

In the discussions of Figures 4 and 5 the total mass concentration, combining original smoke and injected particles, is used as the smoke-reduction criterion, instead of smoke particles only. The reason is because the present objective is to clear the room of all particles. If we introduce new particles to reduce particles originally in the room, the results would not be satisfactory unless all the particles are cleared. For that purpose, there is an issue of selecting an optimal particle size or mass. For some other applications when only the reduction of original smoke is of interest, we need to separately look at the reduction of smoke concentration. The smoke concentration histories are compared in Figures 6 and 7 for the same cases as in Figures 4 and 5. Figures 6 and 7 clearly show the decrease of the smoke particles in all the cases. It is noted that when the slope of any of the injection curves becomes parallel to the no-injection curve, it indicates that the room is out of the injected particles from that moment. In Figures 6 and 7, the 10 μm case has the best performance, at least after approximately 12 min. This is because the number of 10 μm particles is more than that of the larger particles for the same amount of mass, and therefore the chance to capture smoke particles is higher. Although the collision kernel decreases when the size difference between injected and smoke particles decreases, an overwhelmingly large number of particles overweigh the size effect in the kernel. Therefore, if the resulting total particle number in the room is not a concern, this becomes a situation with a monotonic trend where the smaller particles are better for smoke reduction.

DOI: 10.1002/nme

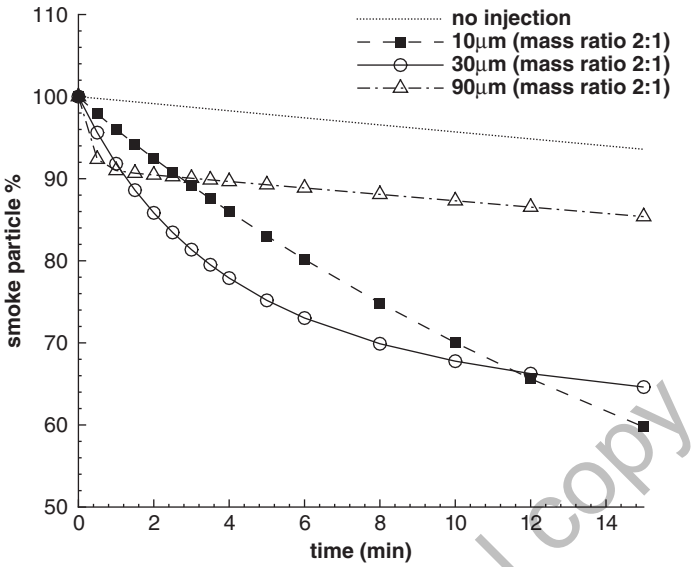

Figure 7. Time history comparison of smoke mass concentration for the case with the injection–smoke mass ratio of 2.

4. CONCLUSIONS

A collision model based on mass balance among the bin structures is developed and successfully validated against the exact solution when the bin volume ratio is large and the inner-bin collision can be neglected. Using this collision model, the computational overhead of the simulation can be reduced significantly and, therefore, enables the integration of the collision simulation with a three-dimensional unsteady turbulent flow solver for smoke-reduction simulation. The smoke-reduction simulation results are compared with the experimental measurement data and good agreement has been achieved. The simulation model has demonstrated the ability in providing important information for determining the optimal injection particle sizes for smoke reduction.

ACKNOWLEDGEMENTS

This work was partially funded through the award of a contract from the United States Marine Corps Systems Command to M2 Technologies Inc.

REFERENCES

1. Yadav R, Maghirang RG, Erickson LE, Kakumanu, B, Castro SG. Laboratory evaluation of the effectiveness of nano-structured materials in clearing smoke in enclosed spaces. *Fire Safety Journal* 2007; DOI: 10.1016/j.firesaf.2007.02.002.
2. Mulukutla R, Malchesky PS, Maghirang RG, Klabunde JS, Klabunde KJ, Koper O. Metal oxide nanoparticles for smoke clearing and fire suppression. *U.S. Patent Application*, 2006.
3. Smoluchowski M. Versuch einer mathematischen theorie der koagulationskinetic kolloider losungen. *Zeitschrift fur Physikalische Chemie* 1917; **92**:129.

DOI: 10.1002/nme

4. Reade WC, Collins LR. A numerical study of the particle size distribution of an aerosol undergoing turbulence coagulation. *Journal of Fluid Mechanics* 2000; **415**:45–64.
5. Gelbard F, Seinfeld JH. Numerical solution of the dynamic equation for particulate systems. *Journal of Computational Physics* 1978; **28**:357–375.
6. Lawler DF, O'Melia CR, Tobiason JE. *Particulates in Water*. American Chemical Society: Washington, DC, 1980; 353–390.
7. Jacobson MZ, Turco RP, Jensen EJ, Toon OB. Modeling coagulation among particles of different composition and size. *Atmospheric Environment* 1994; **28**:1327–1338.
8. Fernandez-Diaz JM, Muniz CG, Brana MAR, Garcia BA, Nieto PJG. A modified semi-implicit method to obtain the evolution of an aerosol by coagulation. *Atmospheric Environment* 2000; **34**:4301–4314.
9. Sandu A. A Newton–Cotes quadrature approach for solving the aerosol coagulation equation. *Atmospheric Environment* 2002; **36**:583–598.
10. Saffman PG, Turner JS. On the collision of drops in turbulent clouds. *Journal of Fluid Mechanics* 1956; **1**:16–30.
11. Williams MMR. A unified theory of aerosol coagulation. *Journal of Physics D—Applied Physics* 1988; **21**: 875–886.
12. Zhang N, Zheng ZC, Glasgow L, Braley B. Particle deposition in a room-sized chamber with particle injection. *Proceedings of ASME Fluid and Engineering Division Summer Conference*, Houston, TX, U.S.A. 19–23 June 2005.
13. Hinds WC. *Aerosol Technology*. Wiley: New York, NY, 1999.
14. Yimer I, Campbell I, Jiang L-Y. Estimation of the turbulent Schmidt number from experimental profiles of axial velocity and concentration for high-Reynolds-number jet flows. *Canadian Aeronautics and Space Journal* 2002; **48**(3):195–200.
15. Zhou L. *Theory and Numerical Modeling of Turbulent Gas-Particle Flows and Combustion*. Science Press: Beijing; CRC Press: Boca Raton, FL, 1993.
16. Zheng ZC, Zhang N. Integral characteristics of mass conservation of particles in flow. *Proceeding of 4th AIAA Theoretical Fluid Mechanics Meeting*, Toronto, Canada, 6–9 June 2005.
17. Shih TH, Liou WW, Shabbir A, Yang Z, Zhu J. A new k–ε eddy viscosity model for high Reynolds number turbulent flows. *Computers and Fluids* 1994; **24**(3):227–238.

DOI: 10.1002/nme